

Contents lists available at ScienceDirect

Journal of the Mechanics and Physics of Solids

journal homepage: www.elsevier.com/locate/jmps





Osmotic instability in soft materials under well-controlled triaxial stress

Zhengjin Wang a,b,*, Junjie Liu b,c, Peijian Chen b,d, Zhigang Suo b,*

- ^a State Key Laboratory for Strength and Vibration of Mechanical Structures, Department of Engineering Mechanics, Xi'an Jiaotong University, Xi'an 710049, China
- ^b School of Engineering and Applied Sciences, Kavli Institute for Bionano Science and Technology, Harvard University, Cambridge, MA 02138, USA ^c Applied Mechanics and Structure Safety Key Laboratory of Sichuan Province, School of Mechanics and Aerospace Engineering, Southwest Jiaotong University, Chengdu, Sichuan 611756, China
- d State Key Laboratory for Geomechanics and Deep Underground Engineering, School of Mechanics and Civil Engineering, China University of Mining and Technology, Xuzhou, Jiangsu 221116, China

ARTICLE INFO

Keywords: Soft materials Triaxial tension Instability Cavitation Fracture

ABSTRACT

Living tissues and some engineering materials contain water. When a wet material loses water, high triaxial tensile stress may build up and cause instability. The mechanism of instability under triaxial tension has attracted great attention, but quantitative study remains an ongoing challenge. Here we develop an experimental method to apply well-controlled triaxial tensile stress and observe osmotic instability in situ. We synthesize a hydrogel in an elastomer tube with strong adhesion between them. The elastomer dissolves minute amount of water, but allows water to diffuse out and places the hydrogel under homogeneous, equal-triaxial, tensile stress. We develop a method to determine the stress as a function of time. The transparent setup enables observation of various types of osmotic instabilities, including cavity nucleation, crack propagation, and surface undulation. Notably, our method enables the measurement of crack speed from $\sim 10^{-5} \, \text{m/s}$ to a limit comparable to the Rayleigh wave speed $\sim 1 \, \text{m/s}$. We observe a large jump in crack speed at a critical energy release rate. This work opens opportunities to study the physics of soft materials under high triaxial tension.

1. Introduction

Osmotic instability is ubiquitous in nature and engineering. Triaxial tensile stress generated by osmosis accumulate elastic energy in materials gradually, and then release the elastic energy rapidly through instability. Examples include embolism in trees (Holbrook and Zwieniecki, 1999), seed dispersal of plants (Noblin et al., 2012; Skotheim and Mahadevan, 2005), and cavitation in microelectronics (Chen and Li, 2011). Triaxial tensile stress can be also generated by decompression (Gent and Tompkins, 1969; Morelle et al., 2021), mechanical stretch (Cristiano et al., 2010; Gent et al., 1959; Lin et al., 2017), thermal mismatch (Nix and Arzt, 1992), and acoustic waves (Rana et al., 2002). Instability induced by triaxial tension may cause decompression sickness (Mahon and Regis, 2014), cerebral contusion (Huang et al., 2019), joint injury (Kawchuk et al., 2015), as well as failure in engineering devices (Nix and Arzt,

 $\textit{E-mail addresses:} \ zhengjinwang@xjtu.edu.cn\ (Z.\ Wang),\ suo@seas.harvard.edu\ (Z.\ Suo).$

^{*} Corresponding authors at: State Key Laboratory for Strength and Vibration of Mechanical Structures, Department of Engineering Mechanics, Xi'an Jiaotong University, Xi'an 710049, China. (Z Wang); School of Engineering and Applied Sciences, Kavli Institute for Bionano Science and Technology, Harvard University, Cambridge, MA 02138, USA. (Z Suo).

1992). To understand these phenomena, many attempts have been made to apply triaxial tension to soft materials (Barney et al., 2020). For example, pulling two rigid plates adhered to the surfaces of a disk of soft material induces an inhomogeneous stress field, with the central part of the soft material under triaxial tension (Cristiano et al., 2010; Gent et al., 1959; Lin et al., 2017). As a second example, gas molecules dissolve in a soft material under high pressure, a rapid decompression builds high stress at flaws, but the magnitude of the stress is hard to calibrate (Gent and Tompkins, 1969; Morelle et al., 2021). As a third example, high triaxial tension has been generated by osmosis and measured through the balance of the chemical potential of water (Wheeler and Stroock, 2008). This method relies on thermodynamic equilibrium, which becomes extremely time-consuming as the size of specimen increases, and cannot determine stress as a function of time. In general, it has been a challenge to apply and measure high triaxial tension in a material and observe instability *in situ*.

We have recently observed some osmotic instabilities in the development of devices using hybrid hydrophilic-hydrophobic polymers (Liu et al., 2020; Yang and Suo, 2018). For example, in an artificial axon, a hydrogel functions like an electrolyte, and a hydrophobic elastomer functions like a myelin sheath (Yang et al., 2015). In a hydrogel-elastomer hybrid, when water molecules in the hydrogel diffuse out through the elastomer, cavities nucleate in the hydrogel and propagate like cracks, and the surfaces of the cracks undulate into a necklace-like shape (Fig. 1a). We also fabricate hydrogel-elastomer hybrids of different geometries and observe various damage pathways (Fig. 1b-c). The hydrogel is soft (shear modulus \sim 10 kPa), but the elastomer is relatively stiff (shear modulus \sim 1 MPa). The elastomer dissolves minute amount of water, but lets water permeate (Le Floch et al., 2017). So long as the hydrogel has a higher chemical potential of water than the environment, water diffuses out of the hydrogel. The hydrogel has a bulk modulus on the order of GPa, much higher than the shear moduli of both the hydrogel and the elastomer. If the hydrogel adheres well to the elastomer, the former is constrained by the latter, and the loss of water builds triaxial tension in the hydrogel.

These observations have intrigued us. Here we design an experimental method to apply well-controlled triaxial stress, determine the stress as a function of time, and observe osmotic instability *in situ*. We synthesize a hydrogel in an elastomer tube (Fig. 2). The hydrogel adheres to the elastomer by covalent bonds. The loss of water places the hydrogel under homogeneous, nearly equal-triaxial, tensile stress. We formulate a theory to determine the stress as a function of time. The transparent setup enables observation of various types of osmotic instabilities, including cavity nucleation, crack propagation, and surface undulation. We quantify the cavitation stress, relate the crack speed and amplitude of surface undulation to the triaxial tensile stress in the hydrogel. This work provides a platform to study the physics of soft materials under high triaxial tension.

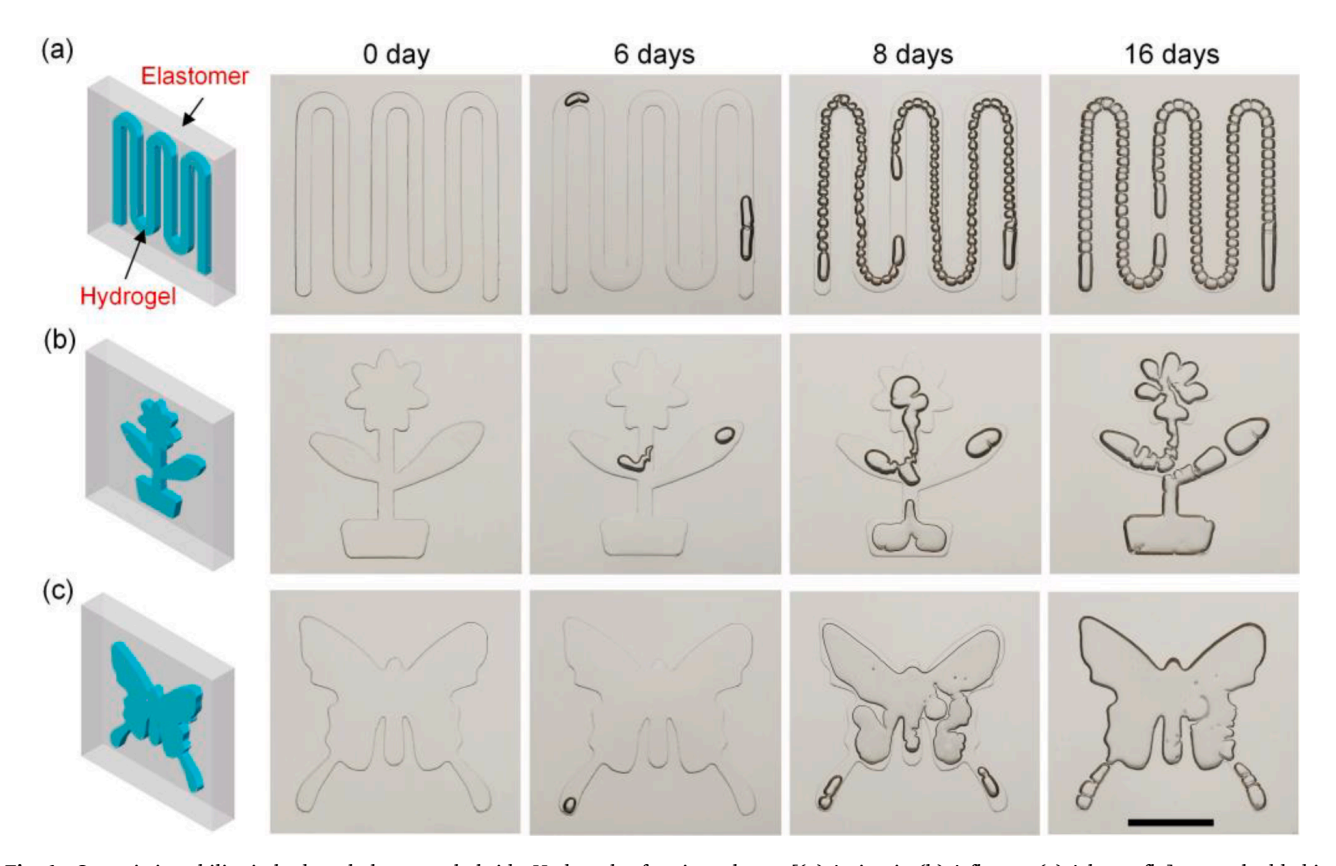


Fig. 1. Osmotic instability in hydrogel-elastomer hybrids. Hydrogels of various shapes [(a) A circuit. (b) A flower. (c) A butterfly] are embedded in elastomers. The hydrogels and elastomers are transparent and adhere by covalent bonds. The hybrids are placed in a chamber of 30% relative humidity, and observed over time. Scale bar, 10 mm.

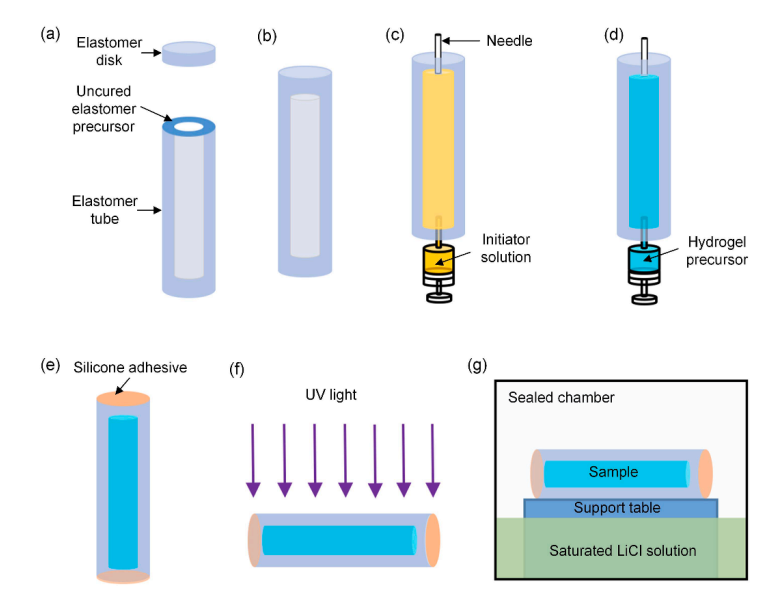


Fig. 2. Sample fabrication and *in situ* observation. (a) A cylindrical tube and a disk of PDMS are made in acrylic molds. (b) Uncured PDMS is used as glue to bond the tube and disk to form a sealed PDMS tube. (c) The inner surface of the PDMS tube is treated with benzophenone solution. (d) The hydrogel precursor is injected into the tube by a syringe. (e) The two ends of PDMS tube are sealed by a layer of silicone adhesive. (f) The sample is cured under UV. (g) The sample is put in a sealed chamber at room temperature, in vapor contact with a saturated solution of lithium chloride.

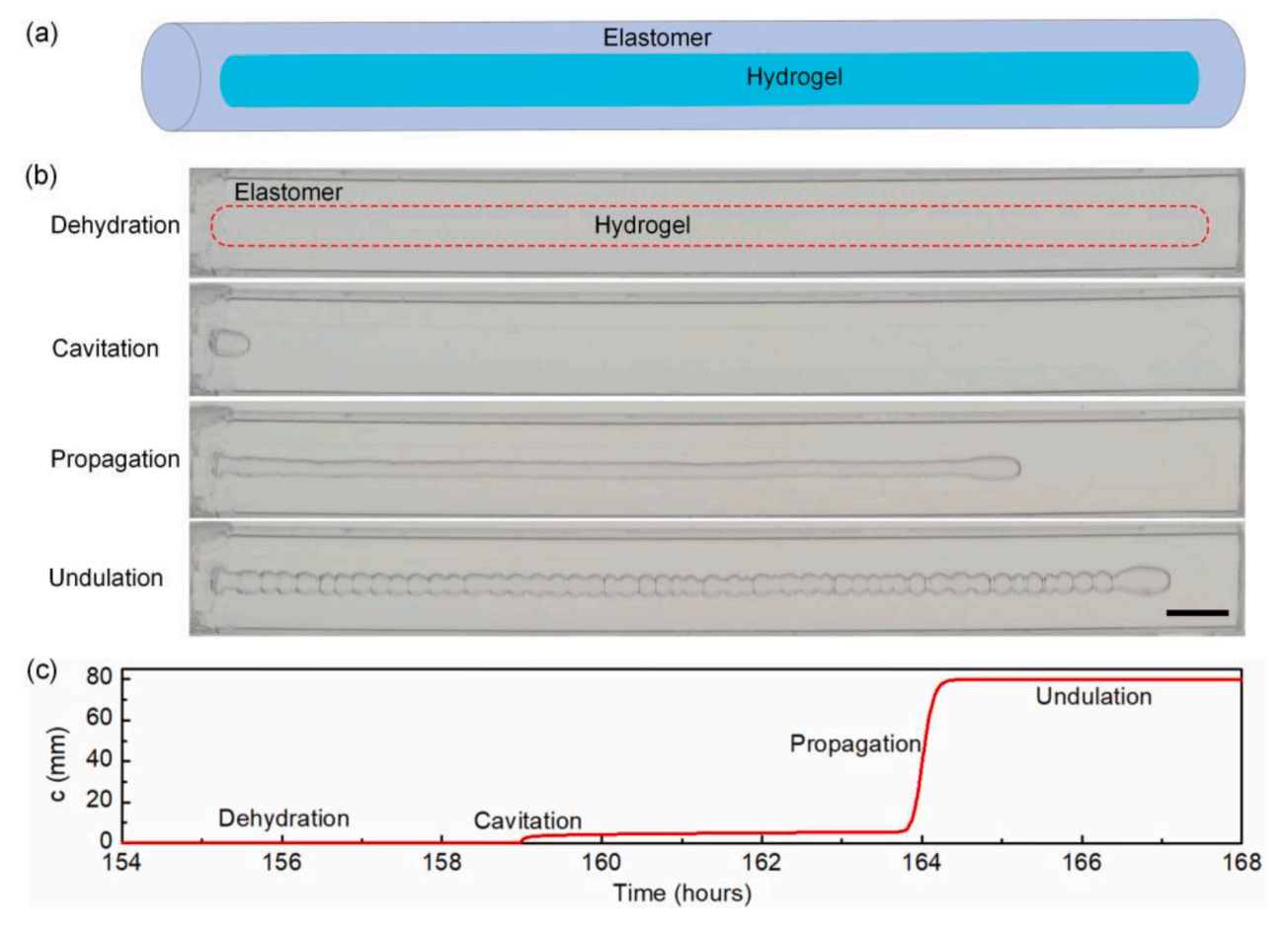


Fig. 3. The observation of a hydrogel in an elastomer tube. (a) The schematic of a hydrogel-elastomer. (b) Snapshots of a sample show four stages: dehydration, cavitation, propagation, and undulation. Scale bar, 5 mm. (c) The length of the cavity or crack as a function of time.

2. Experiments

We first use precursor from Dow Corning (Sylgard 184) to make elastic polydimethylsiloxane (PDMS) tubes. We pour the base and the curing agent of the precursor at a weight ratio of 10:1 into a cup, mix them in a mixer (Thinky ARE-250) at 2,000 r/min for 1 min, and degas at 2,200 r/min for 1 min. We make a PDMS tube of inner radius of 1.5 mm and outer radius of 4.5 mm by pouring the mixture into an acrylic mold, degas the mixture again in a desiccator driven by a vacuum pump, and cure the mixture in an oven at 65 $^{\circ}$ C for 4 h. We make a PDMS disk of thickness of 3 mm and radius of 4.5 mm by a similar procedure using an acrylic mold. We remove the cured PDMS tube and disk from the molds, and then glue the two parts together using the uncured PDMS precursor to form a PDMS tube with two closed ends (Fig. 2a-b).

We next synthesize polyacrylamide (PAAm) hydrogels in PDMS tubes by free-radical polymerization. We dissolve powder of acrylamide (AAm; Sigma-Aldrich, A8887) in distilled water (Poland Spring) to form aqueous solutions, with four concentrations of 1 M (mol/liter), 2 M, 3 M and 4 M AAm/water, dissolve N,N'-Methylenebisacrylamide (MBAA) in distilled water to form 0.1 M MBAA solution as crosslinker, and dissolve 2-Hydroxy-4'-(2-hydroxyethoxy)-2-methylpropiophenone (I2959; Sigma-Aldrich, 410896) in ethyl alcohol to form 0.1 M I2959 solution as photoinitiator. We add 2 µL photoinitiator solution into every 1 ml of AAm solution, add crosslinker at a concentration of 0.2 M (MBAA/AAM) for hydrogel of 1 M AAm concentration, and 0.1 M for hydrogels of 2-4 M AAM concentrations. We achieve strong adhesion between hydrogel and PDMS by forming covalent interlinks using benzophenone as photoinitiator (Sigma-Aldrich, B9300) (Yuk et al., 2016). We use a syringe to inject benzophenone solution (10 wt% in Ethyl alcohol) into the PDMS tube from the bottom end to treat the inner surface for 2 min, another needle is punctured from the top end to expel the air in the tube (Fig. 2c). After the treatment, we inject ethyl alcohol into the tube to wash the inner surface. We then inject the PAAm hydrogel precursor into the PDMS tube from the bottom end, the needle on the top is to expel the air and balance the pressure between inside and outside of the tube (Fig. 2d). The needles are pulled out of the PDMS tube after injection. We use silicone adhesive (3M Super Silicone Sealant 8661, from McMaster-Carr) to heal the small defects introduced by the needles (Fig. 2e). After the silicone adhesive is cured (in 10 min), the sample is put under an ultraviolet lamp (15 W, 365 nm; UVP XX-15L, 10 cm distance between samples and the lamp) for 30 min for the polymerization of PAAm and covalent bonding between PAAm and PDMS (Fig. 2f). We put the sample into a sealed humid box for 24 h to make sure the sample is fully cured. We measure the mass of a sample before and after the injection of the hydrogel precursor to determine the initial mass of the hydrogel.

We put the fully cured sample in a transparent sealed chamber at room temperature (Fig. 2g), in vapor contact with a saturated solution of lithium chloride (Sigma-Aldrich, 310468), which maintains the relative humidity at 11% in the chamber (Young, 1967). We use a low-resolution webcam (Logitech QuickCam Pro 9000, for long time record) to monitor the samples during the experiment, and use a digital camera of high-resolution (Nikon D7000) to take snapshots and record videos during the moment of cavity nucleation, crack propagation, and surface undulation. The length of a crack and the amplitude of crack surface undulation are determined by counting the pixels in the snapshots and videos.

The hydrogel initially dehydrates without instability, but then suddenly forms a cavity (Fig. 3). The cavity is initially a sphere, gradually elongates into a spheroid, and suddenly turns into a tunneling crack. After that, the surfaces of the crack undulate, forming a necklace-like shape. The four stages—dehydration, cavitation, propagation, and undulation—take various amounts of time, depending on experimental variables (Fig. S1 and Videos S1-S3). The video enables us to plot the length of the cavity/crack as a function of time (Fig. 3c).

3. Hydrogel dehydration

When the hydrogel-elastomer hybrid is in a low-humidity environment, water molecules in the hydrogel diffuse out through the elastomer, and the constraint of the elastomer places the hydrogel in triaxial tension (Fig. 4a). We weigh the sample every 1 to 2 days, and determine the ratio of the change in mass to the initial mass of the hydrogel, δ , as a function of time (Fig. 4b). Because the solubility of water in elastomer is extremely low, the loss of water of the hybrid is taken to be entirely from the hydrogel. A total of 31 samples are weighed in the experiment. The measured mass change ratio of the hydrogel is quite repeatable. The diffusion process of water is

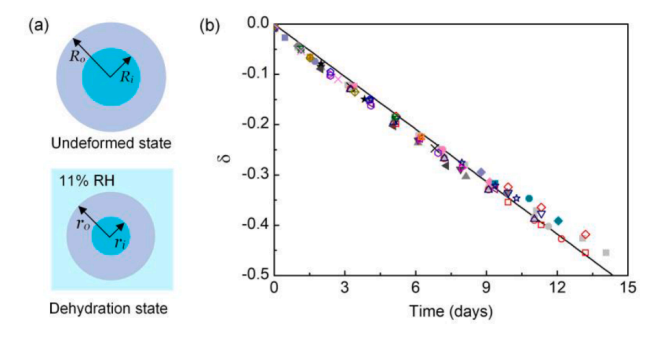


Fig. 4. The mass variation of the hydrogel during dehydration. (a) A cross section of the hydrogel-elastomer hybrid in the undeformed state and a dehydration state in a chamber of 11% relative humidity. (b) A total of 31 samples are weighed over time. The measured change in mass divided by the initial mass of the hydrogel, δ , is plotted as a function of time, and compared with the theoretical prediction (black line).

nonlinear, i.e., the flux of water changes with the variation of elastomer geometry and stress in the hydrogel. We analyze this process theoretically (see Supplementary information for detail). The comparison between analytical and experimental results shows that the nonlinear effect within the range of our experiments is negligible (Fig. S2). For simplicity, the diffusion process can be modeled using the standard partial differential equation of diffusion (Crank, 1975). The elastomer tube separates the hydrogel and environment. The partial pressures of water at the inner and outer surfaces of elastomer tube are Π_1 and Π_2 , respectively. The steady-state flux of water at the hydrogel-elastomer interface is

$$J = \frac{P(\Pi_2 - \Pi_1)}{R_i \ln(R_o/R_i)} \tag{1}$$

where R_i and R_o are the inner and outer radius of elastomer tube in undeformed state. P is permeability of water in elastomer. The mass change rate of the hydrogel is

$$\frac{dM}{dt} = \rho J(2\pi R_i L) = \frac{2\pi \rho P(\Pi_2 - \Pi_1)L}{\ln(R_o/R_i)}$$
(2)

The relative mass change ratio of hydrogel is

$$\delta = \Delta M / M_0 = \frac{2P(\Pi_2 - \Pi_1)}{R_c^2 \ln(R_0 / R_1)} t \tag{3}$$

At room temperature, the relative humidity outside the elastomer is maintained by the saturated lithium chloride solution at 11%, giving a partial pressure of water $\Pi_2 = 0.352$ kPa. The partial pressure of water in the hydrogel can be approximated as that of pure water, $\Pi_1 = \Pi_0 = 3.2$ kPa. The theory agrees with the experimental results very well when *P* is set as 1.75×10^{-16} m²s⁻¹Pa⁻¹, which is comparable to the parameter measured independently (Le Floch et al., 2017).

4. Stress determination

Applying a well-calibrated triaxial tension is in general a challenge, but our experiment does so readily. We develop a method to determine the stress as a function of time. In the as-fabricated state, the hydrogel and elastomer are under the atmospheric pressure, $\sigma = -p_a$. The dehydration causes the hydrogel to shrink in volume, pulls the elastomer tube inward, and builds a triaxial tension in the hydrogel. Because of the abundance of water in the hydrogel, water migrates much faster in the hydrogel than through the elastomer. Consequently, the hydrogel is taken to be homogeneous at all time. Because the shear modulus of the hydrogel is much smaller than that of the elastomer, upon exceeding the shear modulus of the hydrogel, the tension in the hydrogel is nearly equal-triaxial (Fig. S3). When the stress is below a critical value, the elastomer tube deforms axisymmetrically (Cai et al., 2010). We can determine the stress in the hydrogel by solving the boundary value problem of nonlinear elasticity.

Consider a hydrogel cylinder in an elastomer tube, as shown in Fig. 4a. The inner and outer radius of the tube in undeformed state are R_i and R_o , respectively. Because of the low concentration of AAM in hydrogel (the density of AAM = 1.32 g/cm³), the density of hydrogel is very close to that of water. Therefore, during the dehydration process, the mass change ratio of hydrogel, $\delta = \Delta M / M_0$, is equivalent to its volume change ratio, $\Delta V / V_0$. Due to the molecular incompressibility of the hydrogel and elastomer, the deformation state of the hybrid system is determined by the mass change ratio of the hydrogel. Given that the elastomer is much stiffer than hydrogel, the hydrogel-elastomer hybrid is taken to deform under plane-strain condition, i.e., the axial stretch $\lambda_z = 1$. This assumption is confirmed by the experimental observation (Fig. 3b) and finite element simulation (Fig. S3). In deformed state, the inner radius of the elastomer tube becomes r_i , the external radius becomes r_o , and a material particle named after its distance R from the center of tube in undeformed state moves to a place of distance r_o from the center of tube. The elastomer is considered to be incompressible, so

$$(r^2 - r_i^2) = (R^2 - R_i^2)$$
 (4)

By definition the hoop stretch is

$$\lambda_{\theta} = r/R \tag{5}$$

The assumption of incompressibility gives $\lambda_{\theta}\lambda_{r}\lambda_{z}=1$, so that

$$\lambda_r = R/r$$
 (6)

To a high accuracy, the elastomer is modeled as a neo-Hookean material (Fig. S4). The stress and stretch relations are

$$\sigma_r - \sigma_\theta = \mu_e (\lambda_r^2 - \lambda_\theta^2)$$
 (7)

where μ_e is the elastic modulus of the elastomer. Force balance in the cross-section perpendicular to axial direction gives

$$\frac{d\sigma_r}{dr} + \frac{\sigma_r - \sigma_\theta}{r} = 0 \tag{8}$$

The boundary condition is $\sigma_r = -p_a$ when $r = r_o$. Combining Eqs. (4) - (8), along with the boundary condition, we can get

$$\frac{\sigma_r}{\mu_e} = \frac{R_i^2 - r_i^2}{2} \left(\frac{1}{r^2} - \frac{1}{r_o^2} \right) + \ln \frac{Rr_o}{R_o r} - \frac{p_a}{\mu_e} \tag{9}$$

when $r = r_i$, $\sigma_r = \sigma$, σ is the stress in the hydrogel.

$$\frac{\sigma}{\mu_e} = \frac{R_i^2 - r_i^2}{2} \left(\frac{1}{r_i^2} - \frac{1}{\left(R_o^2 - R_i^2\right) + r_i^2} \right) + \ln \frac{R_i \sqrt{\left(R_o^2 - R_i^2\right) + r_i^2}}{R_o r_i} - \frac{p_a}{\mu_e}$$
(10)

The change ratio of mass is

$$\delta = \frac{\Delta M}{M_0} = \frac{\rho \pi (r_i^2 - R_i^2) L}{\rho \pi R_i^2 L} = \left(\frac{r_i}{R_i}\right)^2 - 1 \tag{11}$$

Combining Eqs. (10) and (11) gives

$$\sigma = \frac{\mu_e}{2} \left(\frac{\delta}{\left(R_o/R_i\right)^2 + \delta} - \frac{\delta}{\delta + 1} + \ln\frac{1 + \delta(R_o/R_i)^{-2}}{\delta + 1} \right) - p_a \tag{12}$$

This equation relates the loss of water to the triaxial stress in the hydrogel. We plot the stress in the hydrogel as a function of time (Fig. 5).

5. Cavity nucleation

As the stress in the hydrogel increases, a cavity may nucleate at a random place in the hydrogel (Fig. 6a). Because the mass of hydrogel varies slowly and almost linearly, we measure the mass change of the hydrogel with time before cavitation. The exact time of cavitation is captured by the video, and the cavitation stress is extrapolated from the measured data before cavitation. The cavitation stress varies widely from sample to sample (Fig. 6b). The cavity is approximately a sphere, and its diameter is a fraction of that of the hydrogel cylinder. The nucleation of the cavity is unstable and finished within one second, which is much shorter than the time scale for the diffusion of water. After the initial sudden expansion, the cavity often keeps at a certain size for some time, likely because the cavity has relaxed the surrounding stress. Some samples form cavities when the stress in the hydrogel is compressive, which is understood as follows. In the hydrogel, air bubbles likely exist, with internal pressure equal to the atmospheric pressure of 100 kPa. The stress in the hydrogel is also -100 kPa initially, but will become less compressive by dehydration. This difference in pressure between an air bubble and the hydrogel can cause the air bubble to expand into a cavity.

Our experimental findings shed light on existing theories of cavitation. Cavitation in soft solids has long been observed and modeled (Gent et al., 1959). In early studies, cavitation was considered as a pure elastic process. A cavity forms when a preexisting void expands by elastic deformation at a critical triaxial tensile stress of 2.5 μ . Later it was modified by accounting for the effect of surface tension when the cavity radius a is smaller than the elastocapillary length γ/μ . The dimensionless critical cavitation stress $\sigma_c/\mu=2.5+2\gamma/\mu a$ (Gent and Tompkins, 1970; Kundu and Crosby, 2009). Another perspective views the expansion of a cavity as a fracture process, which starts at a critical stress $\sigma_f/\mu=\alpha\sqrt{\Gamma/\mu a}$, where α is a dimensionless factor, and Γ is the fracture energy of the material (Cristiano et al., 2010; Gent and Wang, 1991; Kundu and Crosby, 2009). It should be noted that in this work the triaxial tensile stress driving the cavity equals $\sigma+p_a$, because of the stress-free state we set. In recent years, great efforts have been devoted to probing the polymer network deformation and damage (Morelle et al., 2021; Ye and Riggleman, 2020), and linking the cavitation and fracture

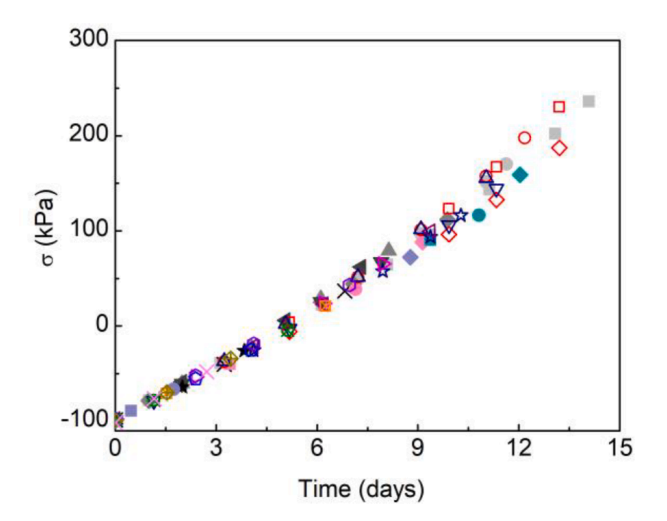


Fig. 5. The stress in the hydrogel. The stress is determined by Eq. (12) based on the measured mass change ratio of hydrogel shown in Fig. 4.

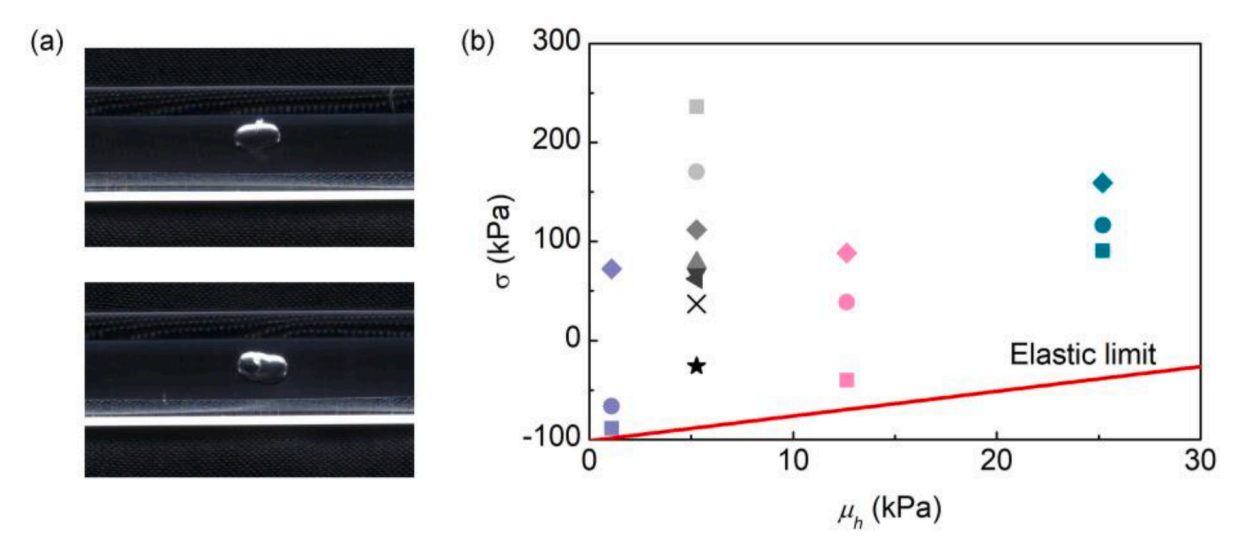


Fig. 6. The cavitation of the hydrogel. (a) The snapshots of cavitated hydrogels. A cavity may nucleate at the interface or inside the hydrogel. (b) The stress for the onset of cavitation, σ, in hydrogels of various shear moduli, μ_h. The four groups of data represent hydrogels of four monomer concentrations varying from 1M to 4M. The elastic limit line is plotted based on the modulus of hydrogel in the as-reacted state.

process (Barney et al., 2022; Kim et al., 2020; Raayai-Ardakani et al., 2019). It has been revealed that the initial growth of a cavity is determined by the ratios of cavity size to the elastofracture and elastocapillary lengths (Barney et al., 2022). When the defect size a is larger than the elastofracture length Γ/μ , the cavity turns into a running crack directly. When $a < \Gamma/\mu$, initially the cavity will expand

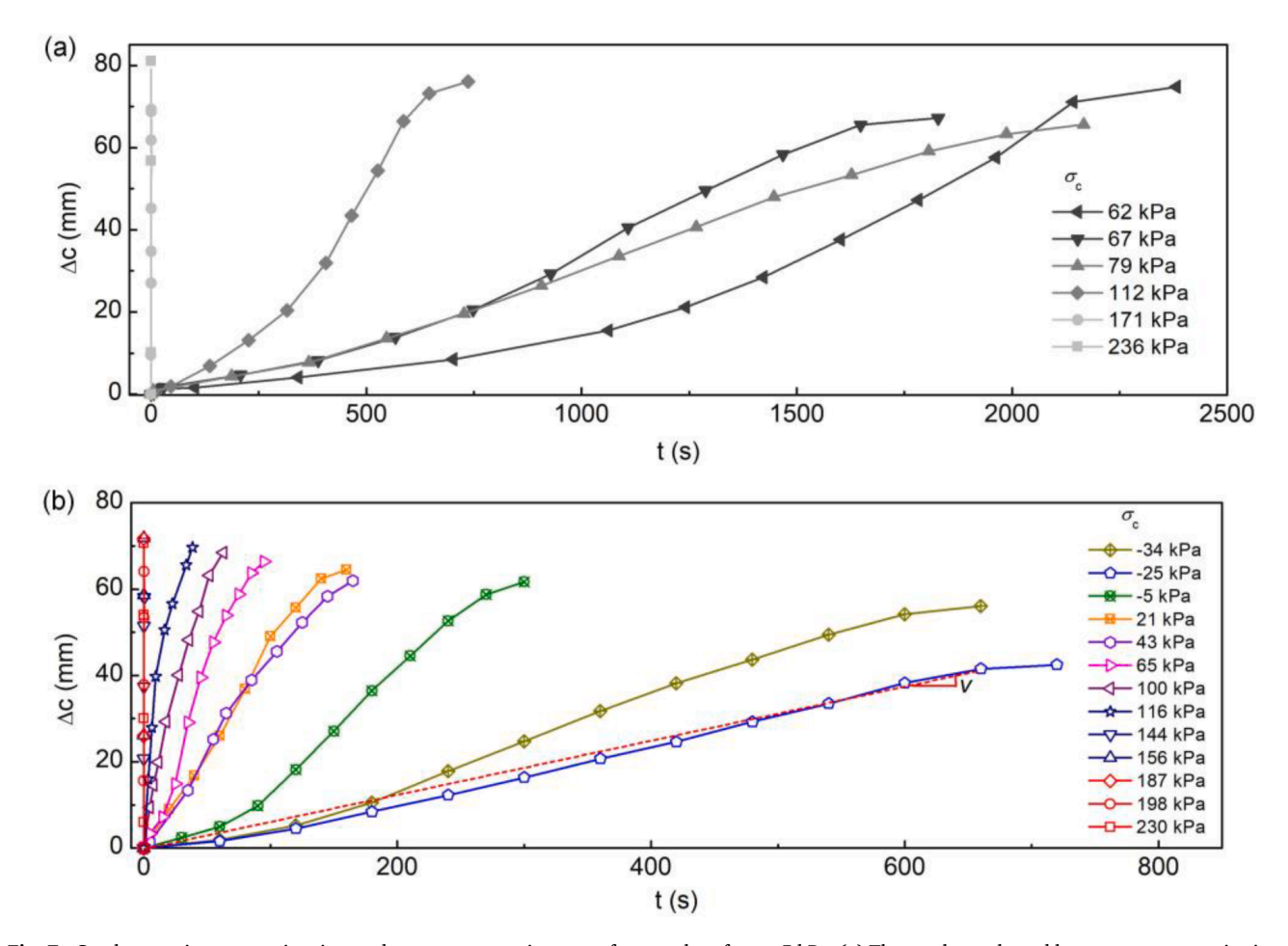


Fig. 7. Crack extension versus time in steady-state propagation stage for samples of $\mu_h = 5$ kPa. (a) The cracks nucleated by spontaneous cavitation. (b) The cracks nucleated by needle puncture. The steady speed of a crack, ν , is defined as the average speed from the moment a crack starts to propagate to the moment the crack runs close to the hydrogel end and slows down quickly (the penultimate point in the curve).

elastically, subsequently it may maintain its shape without any damage, with distributed damage or turning into a running crack, depending on the size of cavity and evolution of driving force during the process of expansion. If a is smaller than the elastocapillary length γ/μ , the initial growth of the cavity is dominated by the surface tension. In our experiment, the elastofracture length of the hydrogels $\Gamma/\mu \sim 10^{-3}$ m. There are no initial defects larger than this length scale observed in our samples. The measured cavitation stresses are way beyond the elastic limit in all cases, indicating that the initial growth of the cavity is resisted by the Laplace stress, 2γ /a. Our observed cavitation stress is on the order of 100 kPa, $\gamma \sim 0.1$ N/m, so the defect size is estimated on the order of $a \sim 10^{-6}$ m. When the cavitation stress is low, the expansion ceases rapidly, the size of the cavity increases by orders of magnitude. This process is probably an elastic-inelastic cavitation process. When the cavitation stress is high, the cavity grows uncontrollably and turns into a crack immediately. The cavity experiences elastic expansion, damage and crack propagation sequentially.

6. Crack propagation

When the cavitation stress is low, the cavity will keep its size, the hydrogel continues to dehydrate to build up tension in the hydrogel away from the cavity, and then the cavity turns into a running crack after some time. When the cavitation stress is beyond a certain value, the cavity turns into a running crack immediately after nucleation (Video S1). We analyze the crack propagation of the samples of $\mu_h = 5$ kPa. Of the eight samples tested, two samples form cavities and do not immediately turn into cracks, and the other six samples form cavities and immediately turn into cracks at a steady speed, ν (Fig. 7a). When the crack tunnels in the sample, the time is too short for the hydrogel to dehydrate significantly, so that the triaxial tension in the hydrogel far ahead of the crack tip changes negligibly. We mark the data points for the six samples on the plane of cavitation stress and crack speed (solid symbols in Fig. 8). We also mark the other two samples on the vertical axis (marked by a black cross and a black star) just to indicate the cavitation stress. A cavity turns into a crack when the stress in the hydrogel exceeds about 60 kPa.

To nucleate a cavity at a controlled stress, we also puncture the hydrogel manually using a syringe needle with a sharp tip at certain time of dehydration (Videos S2 and S3). Of the 14 samples punctured, 13 samples form cracks, and we quantify the crack speed (Fig. 7b) and mark them on the stress-speed plane (hollow symbols in Fig. 8). The other sample does not form crack after puncture, and we mark the stress on the vertical axis (marked by a pink cross). The threshold stress for crack formation is about -40 kPa.

Observe that the threshold stresses for crack formation in the two sets of experiments differ by about 100 kPa, which is the atmospheric pressure. In the cases of spontaneous cavitation, the pressure in the crack drops to almost vacuum state, as its volume increases dramatically within a time scale much shorter than that of air diffusion. In the cases of needle puncture, the syringe needle balances the pressures inside and outside the elastomer.

We unify the two stress-speed curves on the basis of fracture mechanics. We calculate the energy release rate of a crack tunneling in the hydrogel by solving the boundary value problem of nonlinear elasticity (Fig. 9). When a crack tunnels in the hydrogel in steady-state, the stress state near the crack tip is complex, but the deformation fields far ahead and far behind the tip are independent of crack length and keep constant. In the segment far ahead crack tip, the hydrogel is under hydrostatic tension, so the elastic energy in the hydrogel is zero. The elastomer shell is pulled by the hydrogel and stores elastic energy. From the stress analysis above, the elastic energy density in the elastomer tube is:

$$W = \frac{\mu_e}{2} \left(\lambda_r^2 + \lambda_\theta^2 + \lambda_z^2 - 3 \right) = \frac{\mu_e}{2} \left(\frac{r_i^2 - R_i^2}{R^2} - \frac{r_i^2 - R_i^2}{R^2 + R_i^2} \right)$$
 (13)

The elastic energy stored in the elastomer segment far ahead crack tip is:

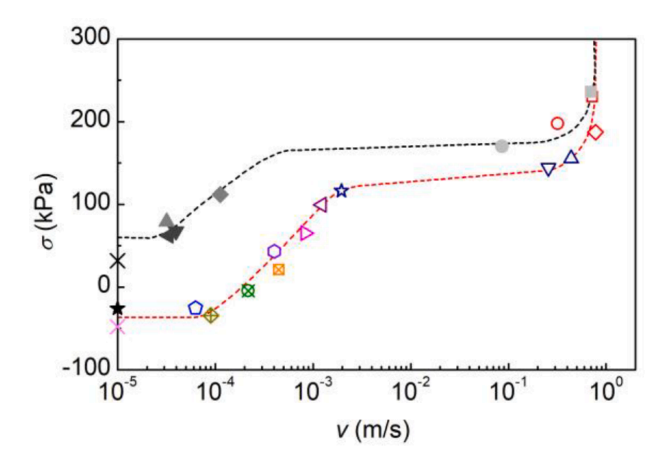


Fig. 8. The relation between cavitation stress and crack speed, ν , for samples of $\mu_h=5$ kPa. Solid symbols represent the cases of spontaneous cavitation. Hollow symbols represent the cases of needle puncture.

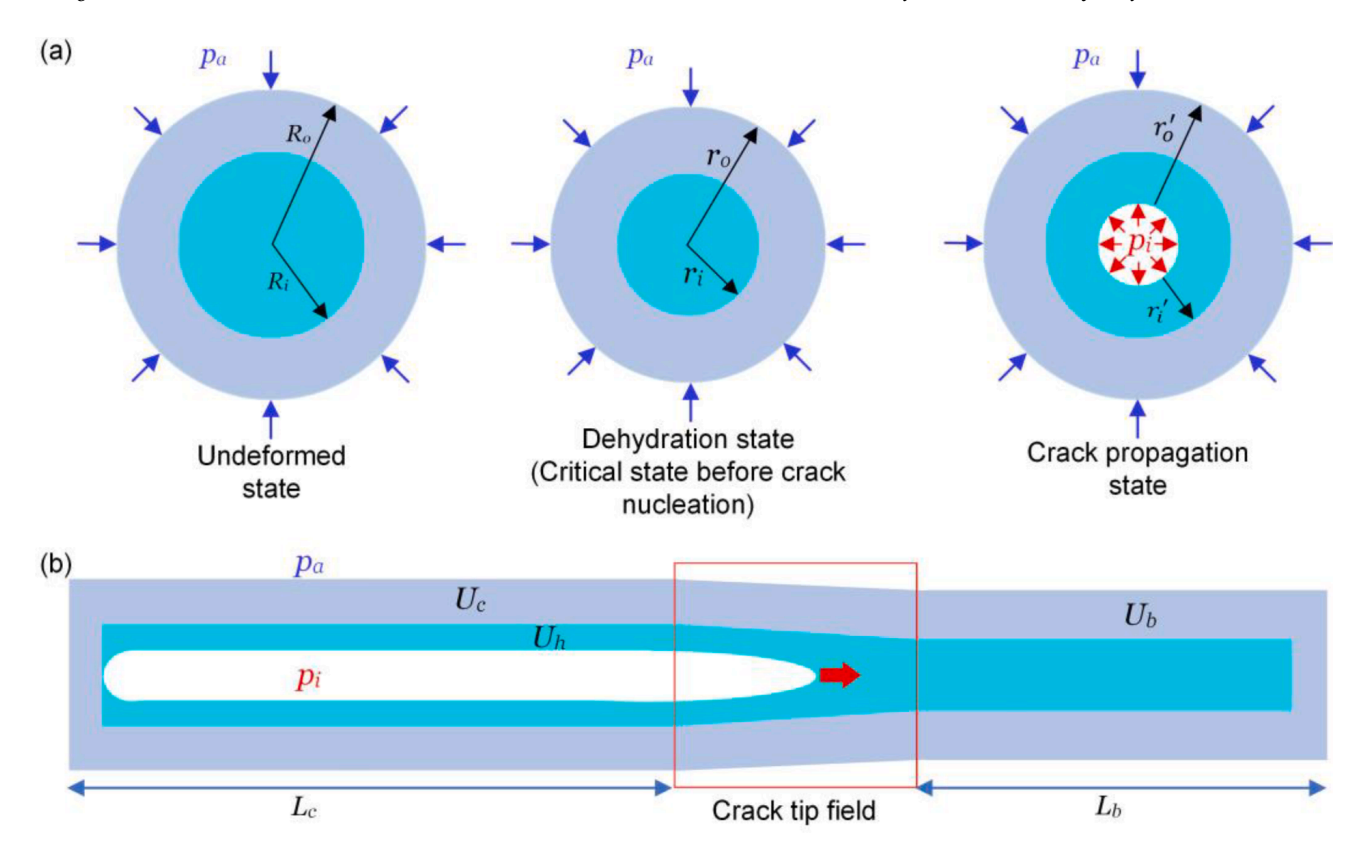


Fig. 9. Schematic of a crack tunneling in a hydrogel-elastomer hybrid. (a) Cross-sections of the hydrogel-elastomer hybrid at different stages. (b) Steady-state crack propagation in the hydrogel-elastomer hybrid.

$$U_{b} = L_{b} \int_{0}^{2\pi} \int_{R_{i}}^{R_{o}} W(R)Rd\theta dR = \frac{\pi \mu_{e} R_{i}^{2} L_{b}}{2} \left[\left(\frac{r_{i}}{R_{i}} \right)^{2} - 1 \right] \ln \left[\frac{(R_{o}/R_{i})^{2} (r_{i}/R_{i})^{2}}{(R_{o}/R_{i})^{2} + (r_{i}/R_{i})^{2} - 1} \right]$$

$$(14)$$

where L_b is the length of the elastomer segment far ahead the crack tip.

After rupture, the elastomer tube pulls the hydrogel to deform outward, the stress in the hydrogel should be at the order of the shear modulus of hydrogel, which is far below the triaxial stress before rupture. So that the elastic energy stored in the hydrogel, $U_h \ll U_b$, which can be neglected. The elastic energy in the elastomer segment far behind the crack tip depends on the pressure difference between the atmosphere pressure, p_a , and the pressure in the crack tunnel, p_i . If the cavitation stress $\sigma < -p_i$, the stress of hydrogel in the fractured segment is compressive, the energy release rate G=0. When the cavitation stress $\sigma > -p_i$, the stress of hydrogel in the fractured segment becomes tensile. The elastic energy stored in the elastomer in ruptured segment is

$$U_{c} = \frac{\pi \mu_{e} R_{i}^{2} L_{c}}{2} \left[\left(\frac{r_{i}'}{R_{i}} \right)^{2} - 1 \right] \ln \left[\frac{\left(R_{o}/R_{i} \right)^{2} \left(r_{i}'/R_{i} \right)^{2}}{\left(R_{o}/R_{i} \right)^{2} + \left(r_{i}'/R_{i} \right)^{2} - 1} \right]$$

$$(15)$$

where r_i is the inner radius of elastomer after rupture, L_c is the length of elastomer tube segment far behind the crack tip, $L_b + L_c =$

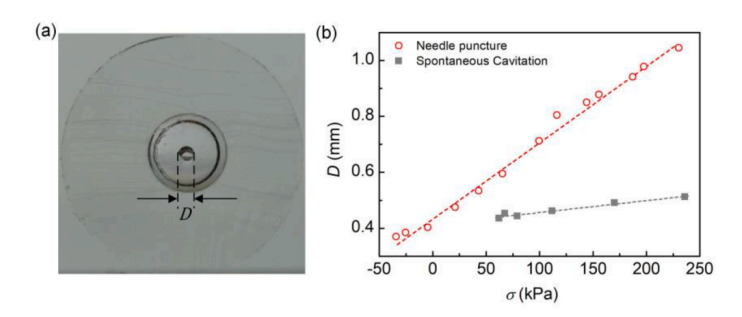


Fig. 10. The size of a crack in the hydrogel. (a) A snapshot of cross-section of a sample after rupture. (b) Crack size versus the stress at which a cavity is nucleated.

constant. The volume of crack tunnel far behind the crack tip is

$$V = \pi (r_i^2 - r_i^2) L_c = \pi R_i^2 L_c (r_i^2 / R_i^2 - \delta - 1)$$
(16)

The elastic energy stored around the crack tip is a constant, U_{tip} . The potential energy of the hydrogel-elastomer hybrid is

$$\Phi(\delta, \Delta p, L_c) = U_b + U_c + U_{tip} - \Delta pV \tag{17}$$

where $\Delta p = p_i - p_a$. The energy release rate of the tunneling crack is:

$$G = -\frac{\partial \Phi(\delta, \Delta p, L_c)}{D \partial L_c} \tag{18}$$

where D is the width of the crack in the undeformed state of hydrogel. We approximate D as the diameter of a crack tunnel measured in the segment cut from a sample after experiment (Fig. 10).

If the crack is nucleated by the puncture of a syringe needle, the pressure inside of the crack tunnel is equal to that of atmosphere pressure, i.e., $p_i = p_0$, so $U_c = 0$. The energy release rate is

$$G_{n} = \frac{\mu_{e} \pi R_{i}^{2}}{2D} \delta \ln \left[\frac{\left(R_{o} / R_{i} \right)^{2} \left(\delta + 1 \right)}{\left(R_{o} / R_{i} \right)^{2} + \delta} \right]$$
(19)

If the crack is initiated by spontaneous cavitation, p_i approaches to vacuum state, which can be approximated as the saturated vapor pressure of water, i.e., $p_i \approx 3.2$ kPa. Substituting pressure, material and geometry parameters into Eqs. (11) and (12), the inner radius of elastomer after rupture becomes $r_i' = 0.9$ R_i , the energy release rate is

$$G_c = G_n + \frac{C_1 \delta + C_2}{D} \tag{20}$$

where $C_1 = 0.693 \text{ J/m}$, $C_2 = 0.063 \text{ J/m}$.

We convert the cavitation stress to the energy release rate of the tunneling crack. The two distinct stress-speed curves collapse into a single curve on the plane of energy release rate and crack speed (Fig. 11). The curve consists of four parts. (I) When the energy release rate is below a threshold, $G_{th} \approx 70 \text{ J/m}^2$, the crack does not form. (II) Above the threshold, as the energy release rate increases, the crack speed increases from 10^{-5} to 10^{-3} m/s gradually. This behavior is commonly attributed to dissipative processes, such as viscoelasticity and poroelasticity (Baumberger et al., 2006; Gent, 1996; Sun et al., 2017). (III) At a critical energy release rate, $G_c \approx 320 \text{ J/m}^2$, the crack jumps to a much higher speed. For rate-dependent materials, like polymers and adhesives, the energy release rate as a function of crack speed, the *G-v* curve, may not be monotonic, but have local minima and maxima (Ciccotti, 2009; Greensmith and Thomas, 1955; Maugis, 1985). As the crack velocity surpasses a critical value, the time scale of kinetics becomes faster than that of dissipative process like viscoelastic relaxation. The dissipative process becomes less and less effective, leading to a drop of *G-v* curve. For higher velocity, the inertia effect involves in and the fracture energy increases again. In our experiment, the energy release rate is constant independent of crack speed, so that the crack jumps when the energy release rate is at a local maximum of the *G-v* curve. This phenomenon is similar to the stick-slip dynamics in adhesive tapes (Ciccotti et al., 2004). (IV) When the energy release rate exceeds G_c , the crack speed is almost a constant, $V \sim 0.8 \text{ m/s}$. This limit speed is around 40% of the Rayleigh wave speed in the hydrogel, $V_R = \frac{0.87+1.12v}{1+v} \sqrt{\mu/\rho} \approx 2 \text{ m/s}$, where $v \sim 0.5$ is the Poisson's ratio of hydrogels (Rahman and Michelitsch, 2006). Dynamic fracture of soft materials has been studied under uniaxial or biaxial tension (Chen et al., 2017; Kolvin et al.,

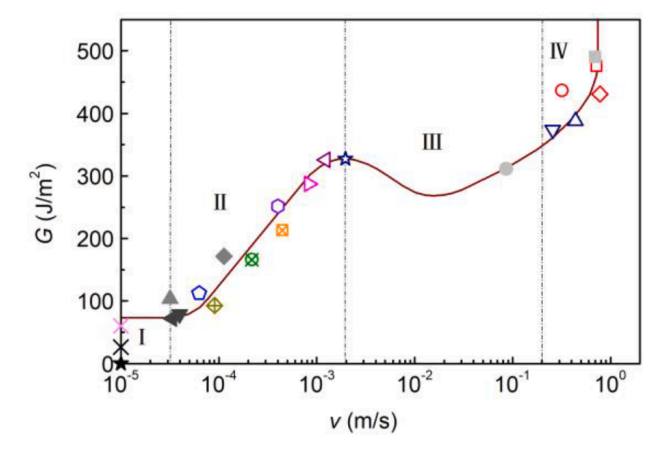


Fig. 11. The relation between energy release rate and crack speed. The two distinct stress-speed curves in Fig. 8 collapse into a single curve. Solid symbols represent the cases of spontaneous cavitation. Hollow symbols represent the cases of needle puncture.

a trigger to launch a crack, with the energy release rate greatly above G_c , driving the crack into this inertia-limited regime. Our experimental method enables fracture of soft materials under high triaxial tension over a wide range of crack speed.

7. Surface undulation

Before a crack forms, the hydrogel is under triaxial tension. Afterward, the crack takes the shape of a cylinder. In many cases, the surface of the tunnel undulates into a necklace-like shape. The amplitude of the undulation grows with time and then plateaus (Fig. 12a and video S3). For the cases cavitated by needle penetration, the undulations form within 10 seconds. In other cases of spontaneous cavitation, they grow slower, from seconds to several hours, which depends on the stress at which the cavity is initiated and the time of air diffusion into the crack tunnel (Fig. S5, see Supplementary information for detail). During the time of undulation, water diffuses through the elastomer negligibly. Consequently, the plateau amplitude is a function of the stress at which the cavity is initiated (Fig. 12b). A threshold stress exists, around 20 kPa, below which the surface of the tunnel does not undulate. The plateau amplitude of undulation increases with stress beyond the threshold, and then keeps almost unchanged with the further increase of cavitation stress. The diameter of the tunnel is in the range between 400 microns and one millimeter (Fig. 10), which is much larger than the elastocapillary length of hydrogel, $\gamma/\mu \sim 10$ microns. Consequently, the undulation is not driven by surface tension (Xuan and Biggins, 2016), but elasticity. Similar elastic instability has been observed in a pressurized tunnel in a soft material recently (Cheewaruangroj et al., 2019). It has been revealed that the surface undulation is a supercritical instability. The wavelength of the undulation is determined by the ratio of the outer radius of the solid to the radius of the tunnel, and its amplitude grows continuously with the increase of pressure.

We focus on the plateau amplitude of undulation in this work. We use a commercial finite-element software, ABAQUS, to calculate the plateau amplitude of undulation based on the elasticity of hydrogels Fig. 13 and Video S4). Before a cavity is initiated, the hydrogel is under hydrostatic tension, without elastic energy storing in it. After rupture, the elastomer almost recovers to undeformed state, and pull the hydrogel to deform outwards. Because the modulus of elastomer is about 100 times that of hydrogels, the effect of elastomer can by simplified as a displacement-controlled expansion applied on the hydrogel. The applied displacement can be converted to the hydrostatic stress prior to crack tunneling by Eqs. (11) and ((12). Given the above-mentioned factors, we only model a hydrogel cylinder of length L=20 mm, Radius R=1.5 mm. The crack tunnel is modeled as a round tunnel with a radius of 0.12R. Axisymmetric model is constructed, and the displacement along axial direction on the two ends is constrained. Radial displacement is applied on the outer radius of the hydrogel. The hydrogel is modelled as a hyperelastic material by neo-Hookean model. An 8-node biquadratic axisymmetric hybrid element (CAX8RH in ABAQUS) is used. A sinusoidal perturbation of tiny amplitude of 1/1000 R and wavelength of 1 mm or 2 mm is prescribed on the tunnel surface. The prediction of the finite element model agrees well with the experimental results, and the wavelength and amplitude of undulation are insensitive to the wavelength of perturbation (Fig. 12b). Because of strong nonlinearity, the simulation is hard to converge when the expansion is too large.

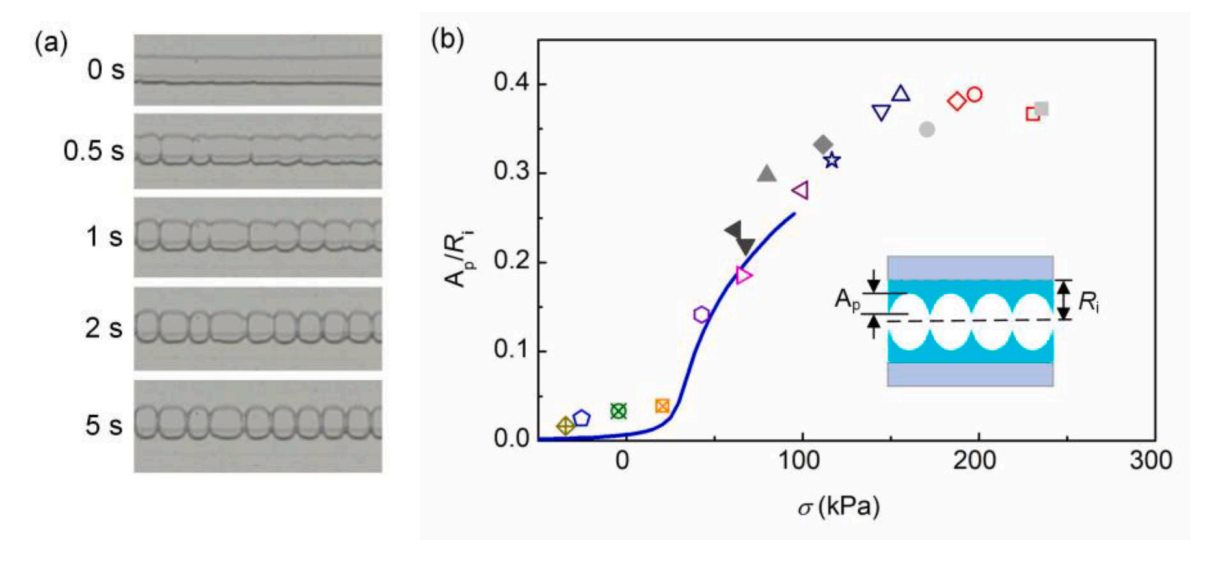


Fig. 12. Surface undulation. (a) the amplitude of undulation increases with time, and then plateau (the snapshots are captured from Video S3). (b) The relation between the normalized plateau amplitude of undulation and the cavitation stress. The blue curve is the result of finite element simulation based on elasticity of hydrogels. Solid symbols represent the cases of spontaneous cavitation. Hollow symbols represent the cases of needle puncture.

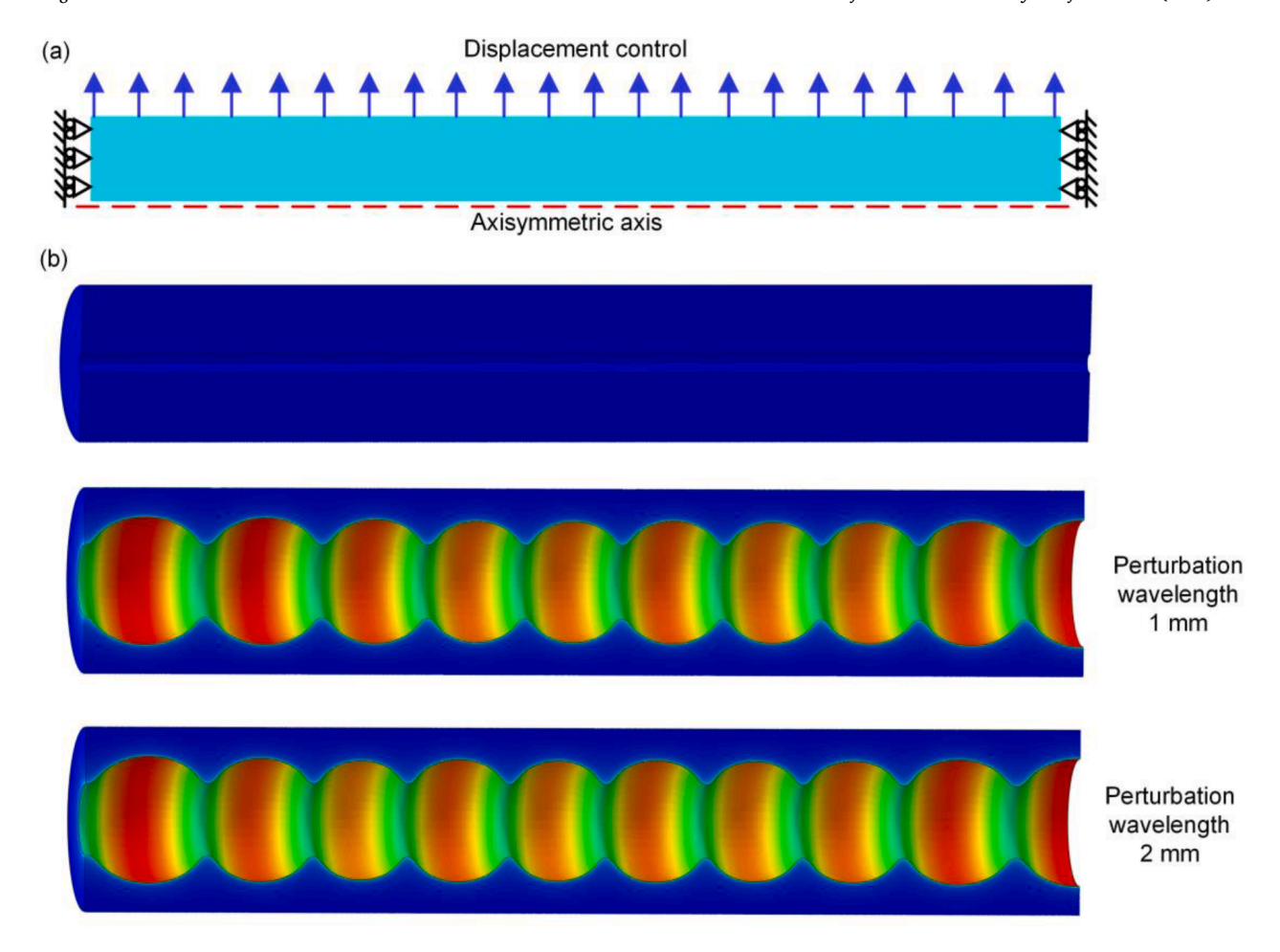


Fig. 13. Finite element simulation of surface undulation. (a) Schematic of the axisymmetric finite element model constructed in ABAQUS. (b) 3D view of the model in undeformed and final state by using sweep function in ABAQUS. The wavelength and amplitude of the undulation are not affected by the input of perturbation wavelength.

8. Discussion

Our method provides a way to apply homogeneous, hydrostatic tensile stress on soft materials and monitor the stress level steadily, which enables the quantitative study of osmotic instabilities. There are still some limitations of the current method, which need to be improved in further studies. First, in current study, we only remove air bubbles in hydrogel precursor by ultrasonic degassing, without any other treatment during fabrication. As a result, the hydrogel cavitates at a random stress beyond a threshold. If experiment at high triaxial tensile stress is desired, many samples may need to be prepared. To make the hydrogel more cavitation-resistant, it is important to remove the air bubbles in the precursor, synthesize hydrogels with homogeneous networks (Sakai et al., 2008; Ye and Riggleman, 2020). After fabrication, some treatments may also help to make the hydrogel resistant to high hydrostatic tension. For example, Wheeler and Stroock use high pressure and high temperature to remove the gas bubbles in porous hydrogel, most of the treated samples can resist as high as 20 MPa of hydrostatic tensile stress without cavitation (Wheeler and Stroock, 2008). Second, even though we can monitor the stress in the hydrogel with time, it is time consuming to reach high stress state. To shorten the dehydration time, a stiffer elastomer is preferred so that the thickness of elastomer tube can be reduced. A higher temperature to increase the dehydration rate may also work (Milner et al., 2017).

9. Conclusions

In this work, we have developed an experimental method to study instability of soft materials under well-controlled triaxial tensile stress. A setup made of hydrogel-elastomer hybrid is designed. The elastomer dissolves minute amount of water but does allow water to diffuse through. The dehydration of hydrogel sets up a homogeneous, nearly equal-triaxial tensile stress field in the hydrogel. The stress is determined on the basis of the loss of water and the elasticity of the elastomer. Both the hydrogel and elastomer are transparent, enabling *in situ* observation of various types of instabilities, including cavity nucleation, crack propagation, and surface undulation. Notably, the capability to apply a homogeneous, equal-triaxial stress on hydrogel enables the steady-state propagation of a crack over a wide range of speed, from $\sim 10^{-5}$ m/s to an inertia-limited speed ~ 1 m/s. It overcomes some limitations of existing

methods and provides a powerful tool to reveal the mechanisms of osmosis-driven dynamic behaviors in nature and failure of engineering materials. In general, this work paves the way to study the physics of soft materials under high triaxial tension.

CRediT authorship contribution statement

Zhengjin Wang: Conceptualization, Methodology, Investigation, Data curation, Formal analysis, Writing – original draft, Funding acquisition. Junjie Liu: Methodology, Formal analysis. Peijian Chen: Investigation, Formal analysis. Zhigang Suo: Conceptualization, Funding acquisition, Resources, Supervision, Writing – review & editing.

Declaration of Competing Interest

The authors declare that they have no known competing financial interests or personal relationships that could have appeared to influence the work reported in this paper

Data Availability

Data will be made available on request.

Acknowledgments

The work at Xi'an Jiaotong University was supported by the National Natural Science Foundation of China (12002255). The work at Harvard was supported by NSF Materials Research Science and Engineering Centers, USA (Grant DMR-2011754). Junjie Liu was supported by China Scholarship Council as a visiting scholar for two years at Harvard University. Peijian Chen was supported by China Scholarship Council as a visiting scholar for one year at Harvard University.

Supplementary materials

Supplementary material associated with this article can be found, in the online version, at doi:10.1016/j.jmps.2022.105195.

References

eaaz0418.

25542-25552

```
Barney, C.W., Dougan, C.E., McLeod, K.R., Kazemi-Moridani, A., Zheng, Y., Ye, Z., Tiwari, S., Sacligil, I., Riggleman, R.A., Cai, S., Lee, J.-H., Peyton, S.R., Tew, G.N.,
   Crosby, A.J., 2020. Cavitation in soft matter. Proc. Natl. Acad. Sci. 117, 9157-9165.
Barney, C.W., Sacligil, I., Tew, G.N., Crosby, A.J., 2022. Linking cavitation and fracture to molecular scale structural damage of model networks. Soft Matter 18,
   4220-4226.
Baumberger, T., Caroli, C., Martina, D., 2006. Solvent control of crack dynamics in a reversible hydrogel. Nat. Mater. 5, 552-555.
Cai, S., Bertoldi, K., Wang, H., Suo, Z., 2010. Osmotic collapse of a void in an elastomer: breathing, buckling and creasing. Soft Matter 6, 5770-5777.
Cheewaruangroj, N., Leonavicius, K., Srinivas, S., Biggins, J.S., 2019. Peristaltic elastic instability in an inflated cylindrical channel. Phys. Rev. Lett. 122, 068003.
Chen, C.-H., Bouchbinder, E., Karma, A., 2017. Instability in dynamic fracture and the failure of the classical theory of cracks. Nat. Phys. 13, 1186-1190.
Chen, Y., Li, P., 2011. The "popcorn effect" of plastic encapsulated microelectronic devices and the typical cases study. In: 2011 International Conference on Quality,
   Reliability, Risk, Maintenance, and Safety Engineering, pp. 482-485.
Ciccotti, M., 2009. Stress-corrosion mechanisms in silicate glasses. J. Phys. D 42, 214006.
Ciccotti, M., Giorgini, B., Vallet, D., Barquins, M., 2004. Complex dynamics in the peeling of an adhesive tape. Int. J. Adhes. Adhes. 24, 143-151.
Crank, J., 1975. The Mathematics of Diffusion, 2nd ed. Clarendon Press, Oxford, UK.
Cristiano, A., Marcellan, A., Long, R., Hui, C.-Y., Stolk, J., Creton, C., 2010. An experimental investigation of fracture by cavitation of model elastomeric networks.
   J. Polym. Sci. B 48, 1409-1422.
Gent, A.N., 1996. Adhesion and strength of viscoelastic solids. Is there a relationship between adhesion and bulk properties? Langmuir 12, 4492-4496.
Gent, A.N., Lindley, P.B., Rideal Eric, K., 1959. Internal rupture of bonded rubber cylinders in tension. Proc. R. Soc. Lond. Ser. A 249, 195-205.
Gent, A.N., Tompkins, D.A., 1969. Nucleation and growth of gas bubbles in elastomers. J. Appl. Phys. 40, 2520-2525.
Gent, A.N., Tompkins, D.A., 1970. Surface energy effects for small holes or particles in elastomers. Rubber Chem. Technol. 43, 873-877.
Gent, A.N., Wang, C., 1991, Fracture mechanics and cavitation in rubber-like solids, J. Mater, Sci. 26, 3392–3395.
Greensmith, H.W., Thomas, A.G., 1955. Rupture of rubber. III. Determination of tear properties. J. Polym. Sci. 18, 189-200.
Holbrook, N.M., Zwieniecki, M.A., 1999. Embolism repair and xylem tension: do we need a miracle? Plant Physiol 120, 7-10.
Huang, A.P.-H., Lai, D.-M., Hsu, Y.-H., Kung, Y., Lan, C., Yeh, C.-S., Tsai, H.-H., Lin, C.-F., Chen, W.-S., 2019. Cavitation-induced traumatic cerebral contusion and
   intracerebral hemorrhage in the rat brain by using an off-the-shelf clinical shockwave device. Sci. Rep. 9, 15614.
Kawchuk, G.N., Fryer, J., Jaremko, J.L., Zeng, H., Rowe, L., Thompson, R., 2015. Real-time visualization of joint cavitation. PLoS One 10, e0119470.
Kim, J.Y., Liu, Z., Weon, B.M., Cohen, T., Hui, C.-Y., Dufresne, E.R., Style, R.W., 2020. Extreme cavity expansion in soft solids: damage without fracture. Sci. Adv. 6,
```

Le Floch, P., Yao, X., Liu, Q., Wang, Z., Nian, G., Sun, Y., Jia, L., Suo, Z., 2017. Wearable and washable conductors for active textiles. ACS Appl. Mater. Interfaces 9,

Lin, S., Mao, Y., Radovitzky, R., Zhao, X., 2017. Instabilities in confined elastic layers under tension: fringe, fingering and cavitation. J. Mech. Phys. Solids 106,

Kolvin, I., Cohen, G., Fineberg, J., 2015. Crack front dynamics: the interplay of singular geometry and crack instabilities. Phys. Rev. Lett. 114, 175501.

Kundu, S., Crosby, A.J., 2009. Cavitation and fracture behavior of polyacrylamide hydrogels, Soft Matter 5, 3963–3968.

Liu, X., Liu, J., Lin, S., Zhao, X., 2020. Hydrogel machines. Mater. Today 36, 102-124.

Maugis, D., 1985. Subcritical crack growth, surface energy, fracture toughness, stick-slip and embrittlement. J. Mater. Sci. 20, 3041-3073.

Milner, M.P., Jin, L., Hutchens, S.B., 2017. Creasing in evaporation-driven cavity collapse. Soft Matter 13, 6894-6904.

Morelle, X.P., Sanoja, G.E., Castagnet, S., Creton, C., 2021. 3D fluorescent mapping of invisible molecular damage after cavitation in hydrogen exposed elastomers. Soft Matter 17, 4266–4274.

Moulinet, S., Adda-Bedia, M., 2015. Popping balloons: a case study of dynamical fragmentation. Phys. Rev. Lett. 115, 184301.

Nix, W.D., Arzt, E., 1992. On void nucleation and growth in metal interconnect lines under electromigration conditions. Metall. Trans. A 23, 2007–2013.

Noblin, X., Rojas, N.O., Westbrook, J., Llorens, C., Argentina, M., Dumais, J., 2012. The fern sporangium: a unique catapult. Science 335, 1322. -1322.

Raayai-Ardakani, S., Earl, D.R., Cohen, T., 2019. The intimate relationship between cavitation and fracture. Soft Matter 15, 4999-5005.

Rahman, M., Michelitsch, T., 2006. A note on the formula for the Rayleigh wave speed. Wave Motion 43, 272-276.

Rana, R.K., Mastai, Y., Gedanken, A., 2002. Acoustic cavitation leading to the morphosynthesis of mesoporous silica vesicles. Adv. Mater. 14, 1414–1418.

Sakai, T., Matsunaga, T., Yamamoto, Y., Ito, C., Yoshida, R., Suzuki, S., Sasaki, N., Shibayama, M., Chung, U.-i., 2008. Design and fabrication of a high-strength hydrogel with ideally homogeneous network structure from tetrahedron-like macromonomers. Macromolecules 41, 5379–5384.

Skotheim, J.M., Mahadevan, L., 2005. Physical limits and design principles for plant and fungal movements. Science 308, 1308-1310.

Sun, T.L., Luo, F., Hong, W., Cui, K., Huang, Y., Zhang, H.J., King, D.R., Kurokawa, T., Nakajima, T., Gong, J.P., 2017. Bulk energy dissipation mechanism for the fracture of tough and self-healing hydrogels. Macromolecules 50, 2923–2931.

Wheeler, T.D., Stroock, A.D., 2008. The transpiration of water at negative pressures in a synthetic tree. Nature 455, 208-212.

Xuan, C., Biggins, J., 2016. Finite-wavelength surface-tension-driven instabilities in soft solids, including instability in a cylindrical channel through an elastic solid. Phys. Rev. E 94, 023107.

Yang, C., Suo, Z., 2018. Hydrogel ionotronics. Nat. Rev. Mater. 3, 125-142.

Yang, C.H., Chen, B., Lu, J.J., Yang, J.H., Zhou, J., Chen, Y.M., Suo, Z., 2015. Ionic cable. Extreme Mech. Lett. 3, 59-65.

Ye, Z., Riggleman, R.A., 2020. Molecular view of cavitation in model-solvated polymer networks. Macromolecules 53, 7825-7834.

Young, J.F., 1967. Humidity control in the laboratory using salt solutions—a review. J. Appl. Chem. 17, 241-245.

Yuk, H., Zhang, T., Parada, G.A., Liu, X., Zhao, X., 2016. Skin-inspired hydrogel–elastomer hybrids with robust interfaces and functional microstructures. Nat. Commun. 7, 12028.